Supporting Information for "Controlled Modification of Superconductivity in Epitaxial Atomic Layer-Organic Molecule Heterostructures"

Shunsuke Yoshizawa,[†] Emi Minamitani,[‡] Saranyan Vijayaraghavan,[§] Puneet Mishra,[§] Yasumasa Takagi,[∥] Toshihiko Yokoyama,[∥] Hiroaki Oba,[⊥] Jun Nitta,[⊥] Kazuyuki Sakamoto,[⊥] Satoshi Watanabe,[‡] Tomonobu Nakayama,[§] and Takashi Uchihashi[§*]*

[†]International Center for Young Scientists (ICYS), National Institute for Materials Science, 1-1, Namiki, Tsukuba, Ibaraki 305-0044, Japan

[‡]Department of Materials Engineering, the University of Tokyo, 7-3-1, Hongo, Bunkyo-ku, Tokyo 113-8656, Japan

[§]International Center for Materials Nanoarchitectonics (MANA), National Institute for Materials Science, 1-1, Namiki, Tsukuba, Ibaraki 305-0044, Japan

[∥]Institute for Molecular Science, Myoudaiji Campus, 38 Nishigo-Naka, Myodaiji, Okazaki, Aichi 444-8585, Japan

[⊥]Department of Nanomaterials Science, Graduate School of Advanced Integration Science, Chiba University, 1-33 Yayoi-cho, Inage-ku, Chiba 263-8522, Japan

E-mail: * YOSHIZAWA.Shunsuke@ nims.go.jp

* UCHIHASHI.Takashi@nims.go.jp

This file contains the following sections.

1. Determination of the assembly structures of MPc monolayers on the Si(111)-(√7×√3)-In surface.

To clarify the assembly structures of MPc monolayers on the (√7×√3)-In surface, STM observations were performed at 4.6 K using a LT STM. In the following, the experimental result and the analysis are described in detail for CuPc. Although the sample bias voltages (V_s) needed to obtain clear STM images were different for the (√7×√3)-In surface and CuPc, comparison of Figs. S1a and S1b taken on the same area allowed us to determine the lattice orientation and the rotational direction of the individual molecules of CuPc monolayers. It was found that the principal axes of the molecular lattice were rotated by 45°from the $[11\bar{2}]$ direction of the Si(111) surface, along which the parallel rows of the (√7×√3)-In surface run (see also Fig. 1d). Since the molecules are closely packed, the center-lobe direction (in-plane mirror axis of CuPc) is rotated by an angle of ~30° from one of the principal axes of the lattice. Consequently, it makes an angle of ~15° against the $[11\bar{2}]$ direction. This observation was always the case as far as the molecular lattice was confined within a single domain region of the (√7×√3)-In surface. This suggests that the orientation of the molecular lattice is locked due to a good commensurability with the underlayer. Indeed, as schematically shown in Fig. S1c, the 3×2 unit cell of the (√7×√3)-In is equivalent to a rectangle with side lengths of 1.995 nm in the $[11\bar{2}]$ direction (≡ $a_{\mathrm{In}[11\bar{2}]}$) and 1.920 nm in the $[\bar{1}10]$ direction (≡ $a_{\mathrm{In}[\bar{1}10]}$). This rectangle is very close in size to the √2×√2 unit cell of the observed molecular lattice

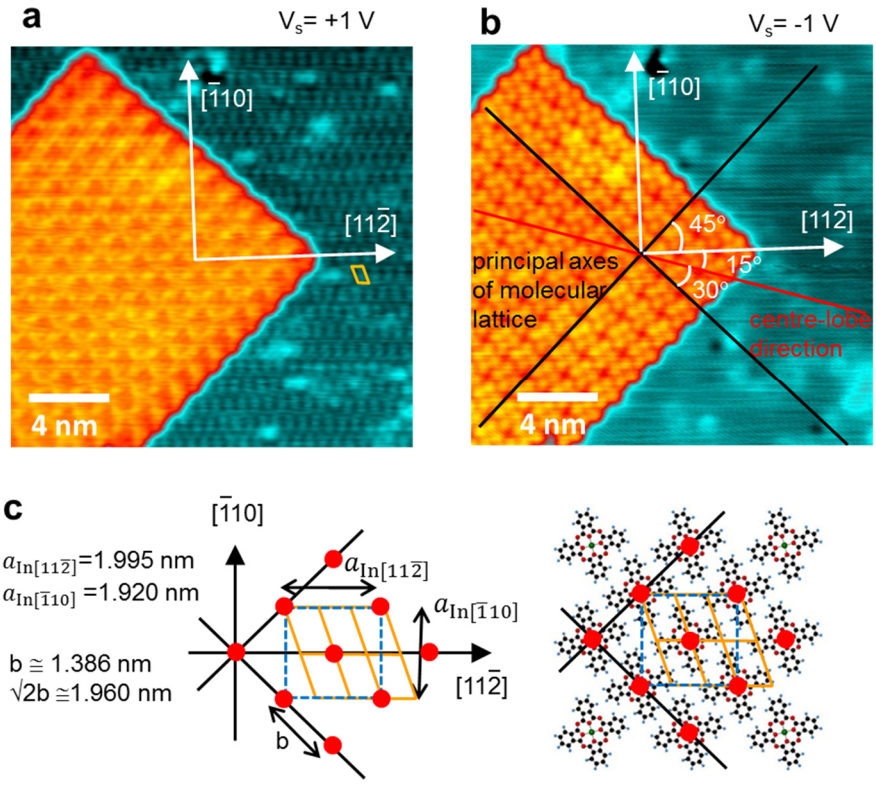

Figure S1. STM images and schematic diagram of a CuPc molecular lattice assembled on the (√7×√3)-In surface. (a)(b) STM images of a monolayer CuPc lattice on the (√7×√3)-In surface taken at 4.6 K ((a): V_s = +1 V, (b): V_s = −1 V). (c) Relation between the CuPc lattice and the (√7×√3)-In surface. Red circles: locations of the CuPc molecules. Yellow lines: the 3×2 unit cell of the (√7×√3)-In. Blue dotted rectangle: the√2×√2 unit cell of CuPc lattices.

(approximately 1.960 nm ×1.960 nm).

More detailed analysis on STM images allowed us to confirm that the commensurability was very good. Figure S2a shows an STM image where both CuPc monolayer islands and the (√7×√3)-In substrate are exposed on the surface. The fast Fourier transform (FFT) patterns of the former and the latter regions are displayed in Figs. S2b and S2c, respectively. The dashed lines indicate the unit cells in the reciprocal space while the blue arrows the unit vectors. Generally, STM images and their FFT patters are deformed due to an error in expansion coefficient calibration of the piezoelectric scanner and to a shear drift caused by thermal drift and creep. However, one can determine the precise periodicity of the CuPc lattice by utilizing the simultaneously observed (√7×√3)-In surface as a reference.

Figure S2d shows a unit cell in the real space with unit vectors $\boldsymbol{a}_1 = (a_{1x}, a_{1y})$ and $\boldsymbol{a}_2 = (a_{2x}, a_{2y})$, while Fig. S2e the corresponding unit cell in the reciprocal space with unit vectors $\boldsymbol{b}_1 = (b_{1x}, b_{1y})$ and $\boldsymbol{b}_2 = (b_{2x}, b_{2y})$. Suppose the unit vectors $\boldsymbol{a}_1$ and $\boldsymbol{a}_2$ are transformed into $\boldsymbol{a'}_1$ and $\boldsymbol{a'}_2$ through expansion

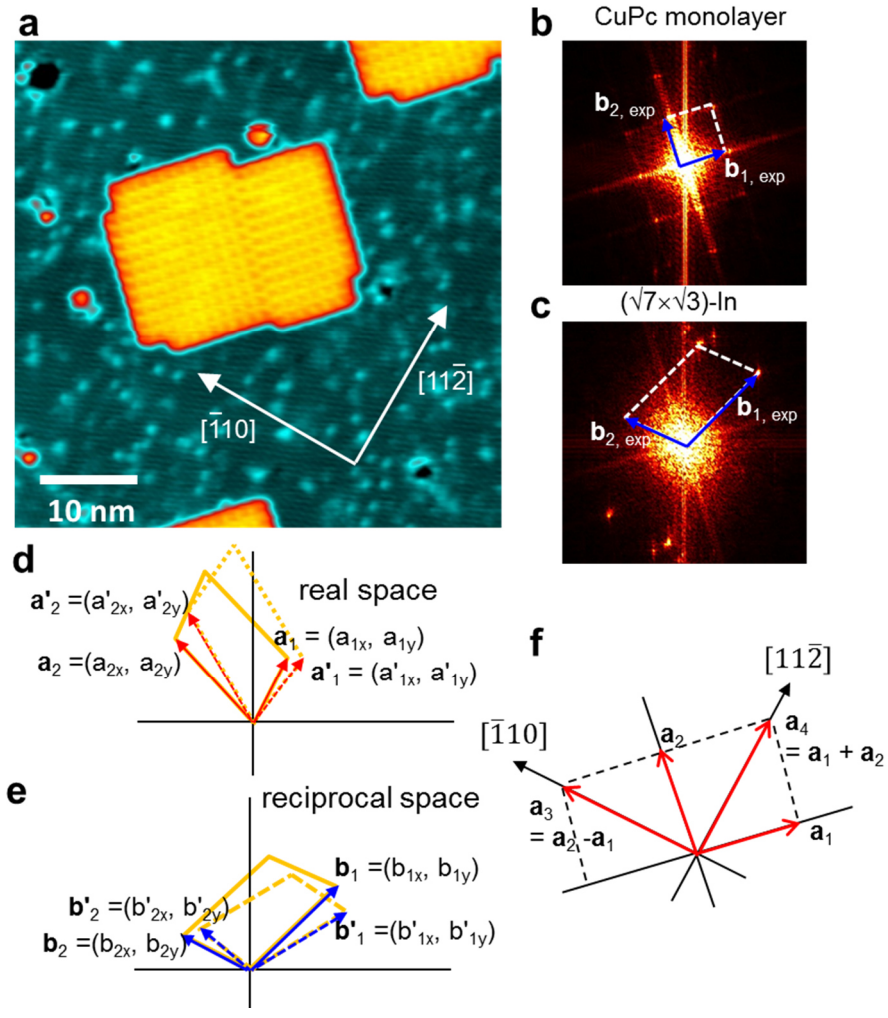

Figure S2. Determination of commensurate relation between the CuPc lattice and the (√7×√3)-In surface. (a) STM image taken at 4.6 K (V_s = +1 V). (b)(c) FFT patterns calculated from the CuPc monolayer region (b) and the (√7×√3)-In region (c) taken from (a). (d)(e) Schematic drawing of a unit cell and unit vectors before and after transformation in real space (d) and receprocal space (e). (f) Relation between vectors $\boldsymbol{a}_1$, $\boldsymbol{a}_2$, $\boldsymbol{a}_3$, $\boldsymbol{a}_4$.

by factors of s, t in the x and y directions ($|s-1|<<1$, $|t-1|<<1$), respectively, shear drift in the x direction by αa_{iy} ($|\alpha|<<1$, i=1,2) and rotation by an angle θ ($|\theta|<<1$) (note that vertical shift in the y direction can be included in expansion in the y direction). Correspondingly, $\boldsymbol{b}_1$ and $\boldsymbol{b}_2$ are transformed into $\boldsymbol{b}'_1$ and $\boldsymbol{b}'_2$. To the first order of $|s-1|$, $|t-1|$, α and θ, one obtains

$$\begin{gathered} b'_{ix}/b_{ix} = 1/s - \theta(b_{iy}/b_{ix}) \\ b'_{iy}/b_{iy} = 1/t - (\alpha-\theta)(b_{ix}/b_{iy}) \\ (i = 1,2). \end{gathered} \tag{1}$$

Hence, s, t, α, θ can be uniquely determined by identifying the experimentally obtained reciprocal unit vectors $\boldsymbol{b}_{i,\,\mathrm{exp}}$ with $\boldsymbol{b}'_i$ (i =1,2).

Analysis using the FFT pattern in Fig. S2c led to s = 0.9888, t = 0.9964, α = −0.0190 and θ = 2.5567°. These parameters were used to correct the unit vectors $\boldsymbol{b}_1$, $\boldsymbol{b}_2$ of the CuPc lattice in Fig. S2b, which were in turn used to determine the unit vectors $\boldsymbol{a}_1$, $\boldsymbol{a}_2$ in the real space. If one defines $\boldsymbol{a}_3 \equiv \boldsymbol{a}_2 - \boldsymbol{a}_1$, $\boldsymbol{a}_4 \equiv \boldsymbol{a}_2 + \boldsymbol{a}_1$ (Fig. S2f), one finds $|\boldsymbol{a}_3|$= 2.009 nm, $|\boldsymbol{a}_4|$=1.977 nm. These values are in agreement with $a_{\mathrm{In}[11\bar{2}]}$ = 1.995 nm and $a_{\mathrm{In}[\bar{1}10]}$ =1.920 nm, respectively, within an error of 3%. Furthermore, the angle made by $\boldsymbol{a}_3$ and $\boldsymbol{a}_4$ is 89.0°, very close to the right angle. Therefore, the CuPc lattice is commensurate with the (√7×√3)-In surface. This means that the CuPc layer is slightly deformed from a perfect square lattice.

The same analysis was applied to other data on the monolayers of CuPc and MnPc. Within an error of ~3%, the obtained values of $|\boldsymbol{a}_3|$ and $|\boldsymbol{a}_4|$ were equal to $a_{\mathrm{In}[11\bar{2}]}$ =1.995 nm and $a_{\mathrm{In}[\bar{1}10]}$= 1.920 nm, respectively. This shows a good commensurability between the MPc molecule lattices and the (√7×√3)-In surface in general and thus rationalizes the observed locking of the molecular lattice direction. The internal molecular structure was not imaged with STM for MnPc in our experiments (see Fig. 1e) because the in-plane $d_{x^2-y^2}$ orbital is located far above the Fermi level (see Fig. 3e) and is not involved in the STM imaging[1]. This precludes a direct determination of the orientation angles of individual MnPc molecules. Nevertheless, they should be identical to that of CuPc (~15° against the $[11\bar{2}]$ direction) considering the close packing and the same lattice constant of the molecule overlayers.

2. Determination of the superconducting transition temperature T_c

Superconductivity in a 2D system generally exhibits a residual resistance near the Bardeen-Cooper-Schrieffer (BCS) condensation temperature, T_c, owing to thermal excitations of free vortices[2]. This makes it difficult to precisely determine T_c. Therefore, the following equation for the 2D resistivity R_{2D} was used to deduce the accurate value of T_c from the fitting of the experimental data[3, 4]:

$$R_{2D}(T) = \left(G_{2D,n}(T) + G_{2D,s}(T)\right)^{-1}, \tag{2}$$

where $G_{2D,n}$ is the normal conductance and $G_{2D,s}$ is the contribution to the conductance due to the superconducting fluctuation effect above T_c. $G_{2D,n}$ was assumed to have the following form:

$$G_{2D,n}(T) = (R_n + \mathrm{a}T^b)^{-1}, \tag{3}$$

where R_n is the residual normal resistance at T = 0 and the temperature-dependent term, $\mathrm{a}T^b$, expresses a power-law behaviour. $G_{2D,s}$ has a temperature dependence given by

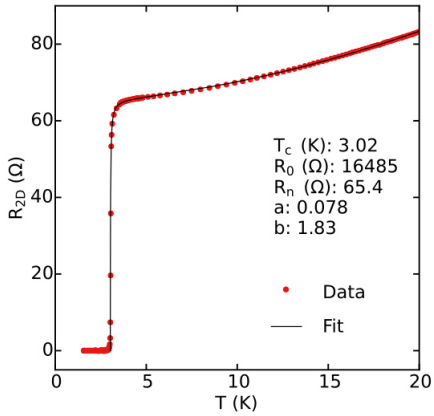

Figure S3. Determination of the superconducting transition temperature T_c.

$$G_{2D,s}(T) = \frac{1}{R_0}\frac{T}{T - T_c}, \tag{4}$$

where the contributions from the Aslamazov-Larkin and the Maki-Thompson terms are included[5, 6]. Precisely speaking, the latter term does not have this form because of the presence of a material-dependent parameter, but it was incorporated into R_0 to reduce the number of fitting parameters[4]. Figure S3 shows an example of the fitting results, from which T_c = 3.02 K and b = 1.83 were obtained.

3. PES measurement of In 4*d* core-levels of the Si(111)-(√7×√3)-In surface

The change in charge states of In atoms and the resulting charge transfer from In to CuPc can be confirmed by the chemical shift of In core-levels through PES measurement. The decrease (increase) in valence electron will reduce (increase) the electrostatic shielding of the nuclear charge from all other electrons. Since the core-level binding energy is determined by the electrostatic interaction

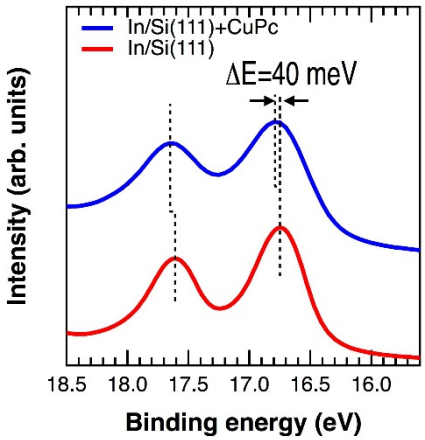

Figure S4. In 4*d* core-levles of the (√7×√3)-In surface (red solid line), and the CuPc the (√7×√3)-In surface (blue solid line) obtained by using $h\nu$ = 40 eV.

between the core electrons and the nucleus, the reduced (increased) shielding shifts the core-level to higher (lower) binding energy. Figure S4 shows the In 4*d* core-levels of the (√7×√3)-In surface and of the CuPc covered (√7×√3)-In surface. As shown in the figure, the In 4*d* core-level shifts 40 meV to the higher binding energy side due to the adsorption of CuPc. This shift indicates a decrease in the density of valence electrons in the In layer, and thus supports the change of the Fermi surface observed in ARPES.

4. XAS/XMCD measurements on MPc molecules on the Si(111)-(√7×√3)-In surface

Note: In this section, θ represents the incident angle of X-ray beam, not the coverage as used in the main text of the paper.

XAS at N *K*-edge

Figure S5a shows the N *K*-edge XAS spectra obtained for a MnPc monolayer on the (√7×√3)-In surface with $\theta = 0°$ and $\theta = 55°$. They exhibit eight peaks similar to those reported for vanadium phthalocyanine[7]. The four peaks on the low- and high-energy sides are attributed to transitions from N 1*s* to π* and σ* molecular orbitals, respectively, both of which have *p* orbital characters [8, 9]. At $\theta = 0°$ the peaks of π* orbitals are negligibly small, while those of σ* orbitals are enhanced. This means

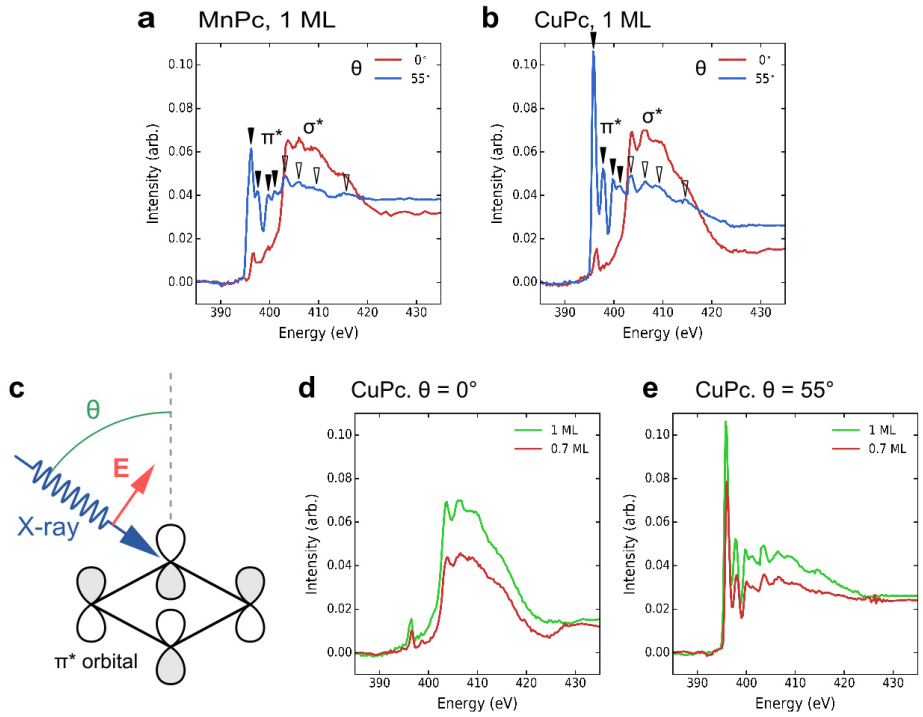

Figure S5. (a)(b) N *K*-edge XAS spectra of MnPc (a) and CuPc (b) monolayers on the (√7×√3)-In surface obtained with $\theta = 0°$ (red) and $\theta = 55°$ (blue). Filled (open) triangles indicate the positions of peaks corresponding to excitations from N 1*s* to π^* (σ^*) molecular orbitals. (c) Schematic illustration for the configuration of the XAS/XMCD measurement of MPc molecules. (d)(e) N *K*-edge XAS spectra of CuPc at $\theta = 0°$ (d) and $\theta = 55°$ (e) measured at different coverages.

that the MnPc molecules were adsorbed in the in-plane geometry, because a dipolar transition from 1*s* to p_z-like π* orbitals is suppressed due to the selection rule when the X-ray beam is in the normal direction (see Fig. S5c). Figure S5b shows the N *K*-edge XAS spectra for a CuPc monolayer, displaying essentially the same spectral features as those of MnPc. This is consistent with the identical adsorption geometries of these MPcs revealed by STM. As shown in Figs. S5d and S5e, the intensity of each peak is approximately proportional to the molecular coverage. The nearly equal XAS intensities for the two MPc monolayers (Figs. S5a and S5b) demonstrate a precise coverage control in the XAS/XMCD experiments.

Details of the sum rule analysis

The effective spin magnetic moment $\langle m_S^{\mathrm{eff}}(\theta)\rangle$ is obtained from the XAS data by using the sum rule [10],

$$\langle m_S^{\mathrm{eff}}(\theta)\rangle = -n_h \frac{9p(\theta) - 6q(\theta)}{r(\theta)}\mu_B, \tag{7}$$

where n_h is the number of holes in the *d* orbitals (assumed to be 5 and 1 for MnPc and CuPc, respectively) and μ_B is the Bohr magneton. The three functions $p(\theta)$, $q(\theta)$, and $r(\theta)$ are given by

$$p(\theta) = \int_{L3} [I^+(E,\theta) - I^-(E,\theta)]dE, \tag{8}$$

$$q(\theta) = \int_{L3,2} [I^+(E,\theta) - I^-(E,\theta)]dE, \tag{9}$$

$$r(\theta) = \int_{L3,2} [I^+(E,\theta) + I^-(E,\theta) + I^0(E,\theta)]dE\,. \tag{10}$$

Here, $I^+(E,\theta)$ and $I^-(E,\theta)$ are the XAS intensities measured with the photon helicity parallel and antiparallel to the applied magnetic field, respectively. $I^0(E,\theta)$ corresponds to the XAS intensity measured with a linear photon polarization parallel to the magnetization, which is approximated as described later. Note that $r(\theta)$ is an isotropic term and thus is independent of θ in principle.

The quantity $\langle m_S^{\mathrm{eff}}(\theta)\rangle$ is composed of two terms:

$$\langle m_S^{\mathrm{eff}}(\theta)\rangle = 2\langle S\rangle + 7\langle T(\theta)\rangle, \tag{11}$$

where $\langle S\rangle$ is the isotropic spin component and $\langle T(\theta)\rangle$ is the intra-atomic dipolar moment. The latter reflects the anisotropic distribution of spins within an atom and, in a system with a symmetry higher than D_{2h}, cancels out at the 'magic angle' of $\theta = 54.7°$[11]. This cancellation of the $\langle T(\theta)\rangle$ term at the magic angle has been demonstrated previously for CuPc and FePc thin films on noble metals[12, 13]. For the discussions on the spin magnetic moments in the main text, we used $\theta = 55°$ to minimize the contribution from the $\langle T(\theta)\rangle$ term.

The $r(\theta)$ term was evaluated differently for MnPc and CuPc. In the cases of MnPc, the angular dependence of $I^+(E,\theta) + I^-(E,\theta)$ is small, and I^0 can be approximated by $I^0 = (I^+ + I^-)/2$. Then, $r(\theta)$ is given by

$$r_{\mathrm{MnPc}}(\theta) = \frac{3}{2}\int_{L3,2} [I^+(E,\theta) + I^-(E,\theta)]dE. \tag{12}$$

For each spectrum, an atomic background was simulated by integrating two Voigt functions placed at the $L_{3,2}$ peaks and was subtracted from the XAS spectrum before applying the sum-rule (Figure S6(a)). In the case of CuPc, a hole is present only in the $d_{x^2-y^2}$ orbital. Owing to its C_4 symmetry, $I^0(E,0°)$ is expected to be zero and $I^+(E,\theta)+I^-(E,\theta)$ has a large angular dependence of the form $f(\theta)=(1+\cos^2\theta)/2$[13]. Hence, $r(\theta)$ for CuPc is given by

$$r_{\mathrm{CuPc}}(\theta)=\frac{1}{f(\theta)}\int_{L3,2}[I^+(E,\theta)+I^-(E,\theta)]dE. \tag{13}$$

Figure S6b shows the $I^+(E,\theta)+I^-(E,\theta)$ of CuPc on the (√7×√3)-In surface, displaying well-separated $L_{3,2}$ peaks. An additional peak labeled as *B* is observed around 940 eV in the curve for $\theta=55°$. This is assigned to the transitions from 2*p* to 4*s* states[14] and disappears at $\theta=0°$. Since the presence of this peak prevents us from defining an atomic background appropriately, we used $r_{\mathrm{CuPc}}(0°)$ instead of $r_{\mathrm{CuPc}}(55°)$ to calculate $\langle m_S^{\mathrm{eff}}(55°)\rangle$. The results of XAS integrations are also plotted by red curves in Figs. S6a and S6b where the small circles indicate the upper bound of the $r(\theta)$ integration range.

Figures S6c and S6d show the XMCD spectra, $I^+(E,55°)-I^-(E,55°)$, and their integrals evaluated for the two MPcs. The integration ranges for $p(\theta)$ and $q(\theta)$ are indicated by the small

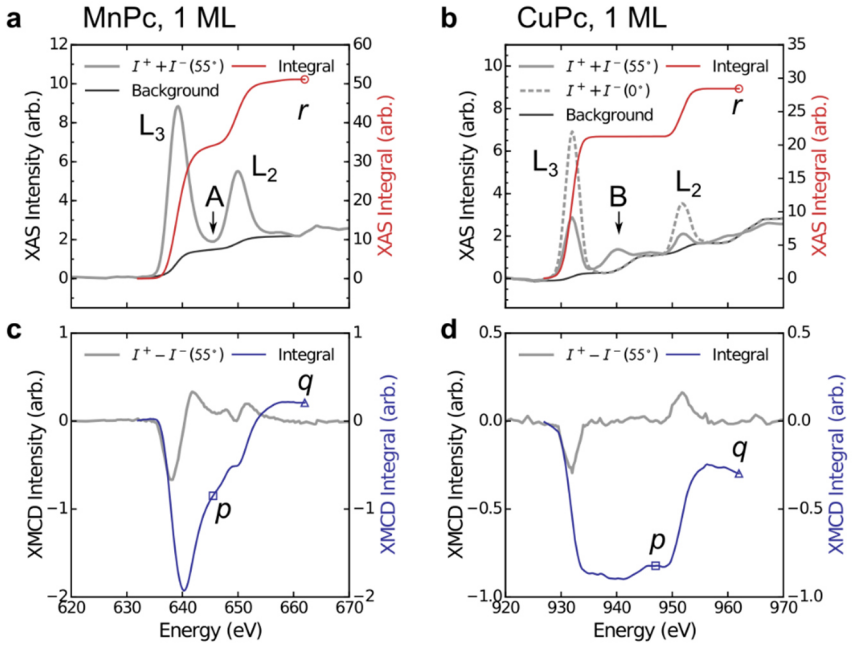

Figure S6. (a)(b) XAS spectra (I^+ + I^-) of MnPc (a) and CuPc (b) at θ = 55° (gray curves). The atomic backgrounds are plotted in thin black curves. The integrals of XAS spectra are plotted in red and the points defining the $r(\theta)$ integration is marked by circles. In the panel (a), the arrow *A* indicates the local minimum of the XAS spectrum used to determine the upper bound of the integration for $p(\theta)$. For CuPc, the XAS integral was calculated from the spectrum for θ = 0° plotted with a gray dashed curve in the panel (b). The small peak labeled as *B* in (b) is related to transitions from 2*p* to 4*s* states. (c)(d) XMCD spectra (I^+ − I^-) of the MnPc (c) and CuPc (d). The points defining the integrations for $p(\theta)$ and $q(\theta)$ are marked by squares and triangles, respectively.

squares and triangles, respectively. In the case of MnPc (Fig. S6c), XMCD signals from $L_{3,2}$ peaks are partially overlapped and the upper bound of the integration for $p(\theta)$ is not obvious. For practical solution, we used the energy at the local minima (labelled as A at 645.5 eV) between the $L_{3,2}$ peaks in the XAS curve (Fig. S6a). If we move this upper bound by ±1 eV, the resulting $\langle m_S^{\mathrm{eff}} \rangle$ value changes by ∓10%. A theoretical study shows that $\langle m_S^{\mathrm{eff}} \rangle$ obtained from a sum-rule analysis on Mn^{2+} is underestimated by 32% [15].

5. *Ab initio* calculations of molecule-induced changes of the electronic states of the Si(111)-(√7×√3)-In surface

In this section, we investigate the effects of the molecule adsorption on the electronic states of the (√7×√3)-In surface through the *ab initio* calculations. Particularly, we focus on the DOS projected on the In p_z orbital of the top-most In layer, which can strongly be coupled to the molecular states because it protrudes in the out-of-plane direction. Figures S7a-e display the projected DOS with the minority (red curve) and majority (blue curve) spins calculated for the surface with and without molecules. The locations of the In atom was selected at the on-site (beneath the metal atom) and at

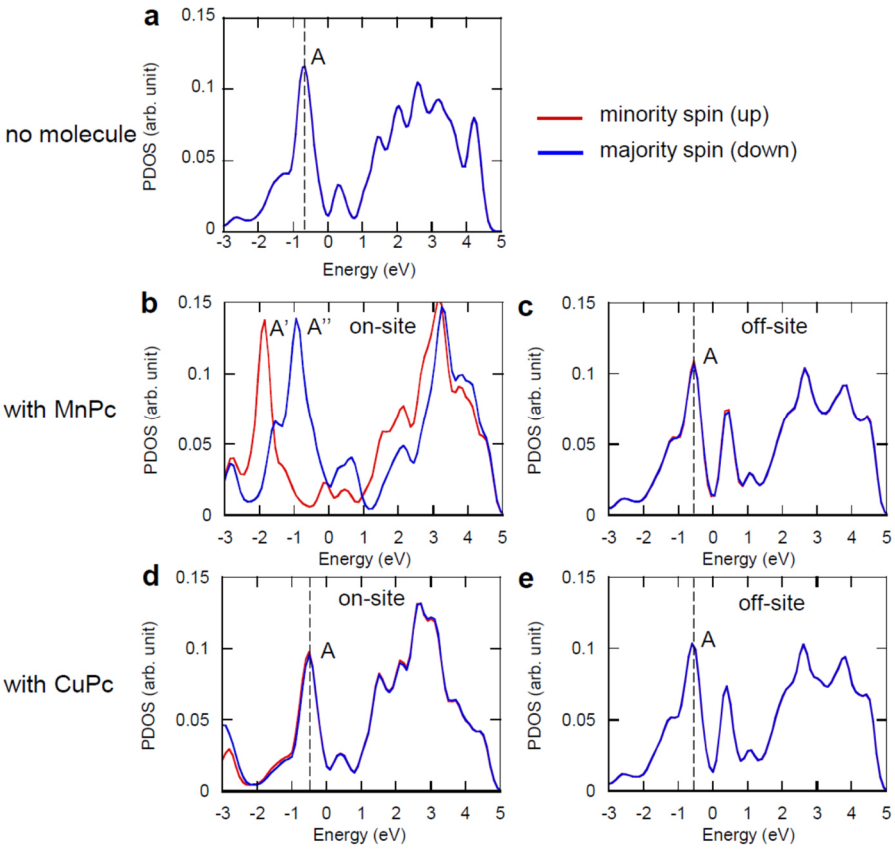

Figure S7. Projected DOS on the In p_z orbital of the top-most layer of the (√7×√3)-In surface with the minority (red curve) and majority (blue curve) spins. The conditions and locations are: (a) no molecule, (b) with MnPc/ on-site, (c) with MnPc/ off-site, (d) with CuPc/ on-site, (e) with CuPc/ off-site.

the off-site (far away from the metal atom). As expected, no spin splitting is found for the (√7×√3)-In surface without molecule (Fig. S7a). A sharp peak labeled as *A* is noticeable around E = -0.8 eV, which was assigned to the In p_z orbital in a previous study.[16] In the case of the MnPc on-site, this peak is largely spin-split into two peaks *A'* and *A*'' together with other spectral features (Fig. S7b), demonstrating the strong spin polarization within the In p_z orbital. This spin polarization is localized beneath the Mn atom, since almost no splitting is visible at the off-site (Fig. S7c). In sharp contrast, nearly no spin splitting is observed in the case of CuPc regardless of the site (Fig. S7c, S7d), indicating a negligibly small effect of CuPc on the spin polarization in the In layer as described in the main text. The MnPc and CuPc adsorptions do not cause a strong change in the spectral shape except at the MnPc on-site, but they shift the energy of the peak *A* in the positive direction by +0.2~0.3 eV. This observation is consistent with the hole doping induced by the charge transfer described in the main text.

References

(1) Mugarza, A.; Robles, R.; Krull, C.; Korytár, R.; Lorente, N.; Gambardella, P. *Phys. Rev. B* **2012,** 85, 155437.

(2) Mooij, J. E., Two-dimensional transition in superconducting films and junction arrays. In *Percolation, Localization, and Superconductivity*, Goldman, A. M.; Wolf, S. A., Eds. Springer: Heidelberg, 1984.

(3) Tinkham, M., *Introduction to Superconductivity*. 2nd ed.; McGraw-Hill: New York, 1996.

(4) Uchihashi, T.; Mishra, P.; Nakayama, T. *Nanoscale Res. Lett.* **2013,** 8, 167.

(5) Aslamasov, L. G.; Larkin, A. I. *Phys. Lett.* **1968,** 26A, 238-239.

(6) Thompson, R. S. *Phys. Rev. B* **1970,** 1, 327-333.

(7) Eguchi, K.; Nakagawa, T.; Takagi, Y.; Yokoyama, T. *J. Phys. Chem. C* **2015,** 119, 9805-9815.

(8) Koch, E. E.; Jugnet, Y.; Himpsel, F. J. *Chem. Phys. Lett.* **1985,** 116, 7-11.

(9) Rocco, M. L. M.; Frank, K. H.; Yannoulis, P.; Koch, E. E. *The Journal of Chemical Physics* **1990,** 93, 6859-6864.

(10) Carra, P.; Thole, B. T.; Altarelli, M.; Wang, X. *Phys. Rev. Lett.* **1993,** 70, 694-697.

(11) Stöhr, J.; König, H. *Phys. Rev. Lett.* **1995,** 75, 3748-3751.

(12) Bartolomé, J.; Bartolomé, F.; García, L. M.; Filoti, G.; Gredig, T.; Colesniuc, C. N.; Schuller, I. K.; Cezar, J. C. *Phys. Rev. B* **2010,** 81, 195405.

(13) Stepanow, S.; Mugarza, A.; Ceballos, G.; Moras, P.; Cezar, J.; Carbone, C.; Gambardella, P. *Phys. Rev. B* **2010,** 82, 014405.

(14) Carniato, S.; Luo, Y.; Ågren, H. *Phys. Rev. B* **2001,** 63, 085105.

(15) Teramura, Y.; Tanaka, A.; Jo, T. *J. Phys. Soc. Jpn.* **1996,** 65, 1053-1055.

(16) Park, J. W.; Kang, M. H. *Phys. Rev. B* **2015,** 92, 045306.